

# Aqueous Manganese-Doped Core/Shell CdTe/ZnS Quantum Dots with Strong Fluorescence and High Relaxivity

Lihong Jing,<sup>†</sup> Ke Ding,<sup>†</sup> Sergii Kalytchuk,<sup>‡,§</sup> Yu Wang,<sup>‡</sup> Ruirui Qiao,<sup>†</sup> Stephen V. Kershaw,<sup>‡</sup> Andrey L. Rogach,<sup>\*,‡</sup> and Mingyuan Gao<sup>\*,†</sup>

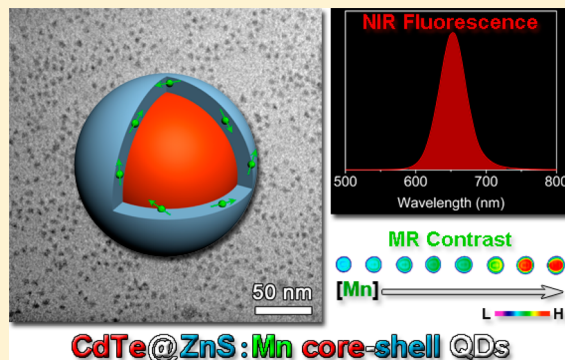
<sup>†</sup>Institute of Chemistry, the Chinese Academy of Sciences, Bei Yi Jie 2, Zhong Guan Cun, Beijing 100190, China

<sup>‡</sup>Department of Physics and Materials Science & Centre for Functional Photonics, City University of Hong Kong, Tat Chee Avenue, Kowloon, Hong Kong S.A.R.

<sup>§</sup>Clean Energy and Nanotechnology (CLEAN) Laboratory, School of Energy and Environment, City University of Hong Kong, Hong Kong S.A.R.

## S Supporting Information

**ABSTRACT:** Core/shell CdTe/ZnS colloidal quantum dots with varying dopant levels (4.7–9.7%) of paramagnetic manganese ions spatially distributed within the thin ZnS shell are synthesized by the aqueous approach. They exhibit both strong fluorescence originating from the CdTe core (up to 45% room temperature emission quantum yield) and high ionic relaxivity in the range of 10.7–5.4 mM<sup>-1</sup> s<sup>-1</sup>, which render them promising dual fluorescent/paramagnetic probes.



## INTRODUCTION

Colloidal semiconductor quantum dots (QDs) doped with transition metal ions have attracted considerable interest as dual fluorescent/paramagnetic probes.<sup>1–6</sup> Fluorescent QDs synthesized by liquid phase-based chemical approaches exhibit useful optical properties such as broad excitation combined with strong, narrow and symmetric emission rendering them suitable as luminescent biomarkers,<sup>7–13</sup> while paramagnetic transition metal ion doping makes them ideal as enhanced contrast agents for magnetic resonance imaging.<sup>14–17</sup> Several strategies for introducing paramagnetic dopants into QDs have been reported,<sup>18–23</sup> including coprecipitation,<sup>24–26</sup> organometallic precursor thermolysis,<sup>28,27</sup> and inorganic cluster precursor thermolysis.<sup>28,29</sup> Following the early research on Mn-doped ZnS QDs by Bhargava,<sup>30</sup> significant progress has been achieved in Mn<sup>2+</sup> doping of both II–VI QDs such as Zn(S,Se)<sup>27,31,32</sup> and Cd(S,Se)<sup>3,33–36</sup> and III–V QDs such as In(P,As).<sup>37–39</sup> For II–VI QDs, substitution of Mn<sup>2+</sup> ions into Zn<sup>2+</sup> sites rather than Cd<sup>2+</sup> sites has been reported as advantageous, due to the intrinsic mismatch between the dopant and host cationic radii for the latter case.<sup>21,29,33</sup> To benefit from the complementary advantages of multifunctional fluorescent/magnetic nanoparticles, it is important to maintain the superior emission characteristics of QDs, something that is not always possible postdoping as introduced dopant impurities often give rise to additional nonradiative decay channels.<sup>31,40,41</sup> One possible solution to minimize the emission quenching involves the

doping of the nanocrystal cores with manganese, followed by epitaxial shell overgrowth on these as-prepared doped cores. This typically results in dopants predominantly located at or near the core–shell interface passivated by the additional shell. This approach has been successfully demonstrated for both Mn-doped isocrystalline core/shell CdS/CdS QDs,<sup>42,43</sup> as well as heterocrystalline core/shell CdS/ZnS,<sup>14,18,42–44</sup> CdS<sub>x</sub>Se<sub>1-x</sub>/ZnS,<sup>45</sup> ZnSe/ZnS,<sup>23,46</sup> and ZnSe/CdSe<sup>47</sup> QDs. Mn doping directly into the shell has been also reported, such as for presynthesized CdSe cores overgrown with Mn-doped ZnS shell, with emission quantum yield up to 20%.<sup>15</sup>

Most of these QDs have been synthesized by organic phase thermal decomposition of suitable precursors at high temperature, which requires additional postsynthetic phase transfer procedures for their anticipated use in aqueous phase biological applications. Direct aqueous phase synthetic approaches for strongly emitting II–VI QDs doped with paramagnetic Mn<sup>2+</sup> ions are highly desirable, and we have addressed this demand in the present work by choosing strongly emitting CdTe QDs<sup>48–50</sup> as a core material on which to deposit a wide-bandgap semiconductor ZnS shell with paramagnetic manganese dopant ions. The ZnS shell provides a suitable matrix for manganese doping and at the same time maintains the high

Received: June 27, 2013

Revised: August 4, 2013

Published: August 28, 2013



fluorescence efficiency and enhances the chemical stability of the CdTe core.<sup>50,51</sup> The incorporation of Mn<sup>2+</sup> ions into the growing ZnS shell has been accomplished by their coprecipitation with Zn<sup>2+</sup> ions using glutathione (GSH) tripeptide as a sulfur source. The latter is both a ligand and releases sulfide ions during its thermal decomposition. The optical and magnetic properties of the resultant Mn-doped CdTe/ZnS core–shell QDs have been systematically studied as a function of variable amounts of Mn<sup>2+</sup> dopant ions.

## ■ EXPERIMENTAL SECTION

**Chemicals.** Cadmium perchlorate hexahydrate (Aldrich, 99.9%), thioglycolic acid (TGA; Fluka, 97%+), 3-mercaptopropionic acid (MPA; Aldrich, ≥99.0%), L-glutathione reduced (GSH; Sigma-Aldrich, ≥98.0%), manganese(II) chloride (Aldrich, 98%), and zinc chloride (Fluka, ≥97.0%) were used as received. Octadecyl-p-vinylbenzyl-dimethylammonium chloride (OVDAC) was synthesized according to Aoyagi et al.<sup>52</sup>

**Synthesis of CdTe Core QDs.** CdTe QDs were synthesized according to the previously reported method.<sup>53,54</sup> Briefly, 1.262 g of Cd(ClO<sub>4</sub>)<sub>2</sub>·6H<sub>2</sub>O (3.01 mmol) was dissolved in 160 mL of water, and 0.371 g of TGA (3.91 mmol) was introduced under stirring. The pH value of the reaction mixture was adjusted to 12.00 by dropwise addition of 1 M NaOH aqueous solution, followed by deaeration under nitrogen flow for 1 h. H<sub>2</sub>Te gas (note: H<sub>2</sub>Te gas is highly flammable and toxic by inhalation), generated by dropwise addition of 13 mL of 0.5 M H<sub>2</sub>SO<sub>4</sub> into an oxygen-free flask containing 0.257 g (0.589 mmol) of Al<sub>2</sub>Te<sub>3</sub> lumps, was introduced into solution driven by a slow stream of N<sub>2</sub>. The resultant solution was refluxed under open-air conditions, until CdTe QDs reached the desired size.

**Synthesis of CdTe/ZnS and Manganese-Doped CdTe/ZnS Core/Shell QDs.** The precursor solution for ZnS shell growth was prepared by dissolving ZnCl<sub>2</sub> (2.66 mmol/L), GSH (1.06 mmol/L), and MPA (4.26 mmol/L) in water, followed by pH adjustment to 9.5 by the dropwise addition of 1 M NaOH. The precursor solution for deposition of the ZnS shell doped with manganese ions was prepared in the same way, with the further addition of appropriate amounts of Mn<sup>2+</sup> ions. Three molar ratios of Mn<sup>2+</sup>-to-Cd<sup>2+</sup> ions (defined as the molar ratios of Mn<sup>2+</sup> precursor introduced into the reaction mixture to the amount of Cd in the CdTe QD core determined by compositional analysis) were used, namely: 0.108, 0.171, and 0.297. As-prepared CdTe core QDs were precipitated by isopropanol and introduced into precursor solutions at a concentration of 3.12 × 10<sup>-6</sup> mol/L. After deaerating by nitrogen bubbling for 30 min, the mixture was heated to reflux under open-air conditions, and the progress of the reaction was monitored by absorption and fluorescence spectroscopy.

**Structural and Compositional Characterization.** Transmission electron microscopy (TEM) and high resolution TEM (HRTEM) images were recorded with a Philips CM 200 FEG microscope and a FEI Tecnai20 JEM-2100F microscope, respectively. Samples for TEM were prepared by drying a drop of diluted QD solution in toluene on the copper grids coated with a thin carbon film. To achieve better contrast and avoid aggregation on the grids, QDs were transferred from water into toluene utilizing OVDAC as a phase transfer agent according to Zhang et al.<sup>55</sup> Powder X-ray diffraction (XRD) patterns of the QD samples on glass substrates were recorded on a Regaku D/Max-2500 diffractometer. The composition of Mn-doped QDs was determined by an inductively coupled plasma optical emission spectrometer (ICP-OES) using a

Thermo Fisher IRIS Intrepid II XSP. Samples for elemental analysis were prepared by decomposition of QDs in a HCl/HNO<sub>3</sub> mixture (aqua regia) with subsequent dilution by Milli-Q water. The manganese doping levels, defined as [Mn]/([Mn] + [Cd]<sub>CdTe</sub> + [Zn]), were evaluated after three cycles of precipitation of QDs with isopropanol, centrifugation, and redissolution in water, followed by further purification by filter dialysis on a 10-K MWCO centrifugal device (Millipore YM-10) against an aqueous medium solution containing MPA (4.8 mmol/L) for ligand exchange at pH 9.5 in order to elute the excess surface ligand bound Mn<sup>2+</sup> ions. The same purification procedure was applied to the samples for electron paramagnetic resonance (EPR) studies. X-ray photoelectron spectroscopy (XPS) was performed on an ESCALAB 220i-XL photoelectron spectrometer (VG Scientific). The binding energies for different elements were calibrated with respect to the C1s line at 284.8 eV from adventitious carbon. A combination of a Shirley type background and a linear background was used for spectral curve fitting.

**Spectroscopic Characterization.** Steady-state UV-vis absorption and photoluminescence spectra were recorded at room temperature on a Cary 50 UV-vis spectrophotometer and a Cary Eclipse fluorescence spectrophotometer, respectively. The photoluminescence quantum yield (PL QY) of QD solutions was estimated using Rhodamine 6G as a fluorescence standard. The excitation wavelength for all steady-state PL spectra was 400 nm. Time-resolved photoluminescence spectra were measured on an Edinburgh Instruments FLS920P spectrometer, with a picosecond pulsed diode laser (EPL-405 nm, pulse width: 49 ps) as a single wavelength (405 nm) excitation light source for the time-correlated single-photon (TCSP) counting measurements.

**Magnetic Characterization.** EPR spectra were recorded at room temperature on a Bruker ELEXSYS E 500 X-Band spectrometer equipped with a ST4102 cavity. Typical experimental conditions were as follows: frequency 9.78 GHz, microwave power 10.11 mW, time constant 40.96 ms, center field 3480 G, modulation frequency 100 kHz, resolution 1024 points, sweep width 1000 G, average of 6 scans. Manganese doped QDs were further characterized by magnetic resonance (MR) relaxivity measurements on a 3 T clinical MRI instrument (GE signa 3.0 T HD, Milwaukee, WI). The parameters for T<sub>1</sub> measurements were set as follows: echo time (TE) = 25.3 ms; repetition time (TR) = 500, 1000, 1500, and 2000 ms; number of excitations (NEX) = 8. The longitudinal relaxivity (*r*<sub>1</sub>) was determined as the slope of the line for plots of 1/T<sub>1</sub> against increasing manganese ion and QD particle concentration, with a correlation coefficient greater than 0.98.

## ■ RESULTS AND DISCUSSION

**Synthesis and Characterization of Core/Shell QDs.** To monitor the optical properties of the CdTe QDs (core PL emission maximum at 610 nm with a PL QY of 45%) during the ZnS shell formation and the manganese doping process, both absorption and fluorescence spectra were followed during the reaction time (Figure 1). As observed for both undoped (Figure 1a) and Mn-doped CdTe/ZnS QDs where the initial molar ratio of Mn<sup>2+</sup>-to-Cd<sup>2+</sup> ions was 0.108 (Figure 1b), the gradual increase in absorbance across the whole spectral range of the CdTe QDs accompanied by a progressive red shift of the band edge is consistent with the formation of a wide bandgap ZnS shell over the narrower bandgap CdTe core rather than with the formation of Cd<sub>x</sub>Zn<sub>1-x</sub>Te alloy QDs. The emission

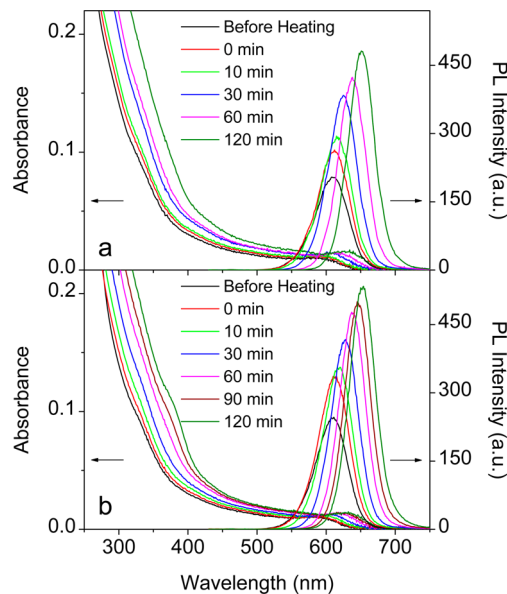


**Figure 1.** Temporal evolution of the absorption and PL spectra of (a) undoped CdTe/ZnS QDs and (b) Mn-doped CdTe/ZnS QDs with the initial feed molar ratio of Mn<sup>2+</sup>-to-Cd<sup>2+</sup> of 0.108 recorded for different reflux times as indicated.

peak of CdTe QDs in both cases also shifted to the red, tracking the red shift in the absorption band edge. For the undoped CdTe/ZnS QDs, the PL QY increased to 52% after 30 min of reflux followed by a decrease to 39% after 2 h of reflux (Figure 1a), while for the Mn-doped CdTe/ZnS QDs, the PL QY increased to 62% after only 10 min of reflux followed by a decrease to 45% after 2 h of reflux (Figure 1b). The increase in the PL QY is often caused by the elimination of surface defects after the deposition of a wide bandgap semiconductor shell on the lower bandgap core,<sup>56,57</sup> while its subsequent decrease can be due to the increasing (compressive) strain at the interface between the core and the thickening shell,<sup>58</sup> originating from the relatively large lattice mismatch (~17%) between CdTe and ZnS.<sup>59</sup> Another important indication for the formation of a core/shell structure was observed in the PL excitation (PLE) and PL emission spectra at different excitation wavelengths (Supporting Information (SI), Figure S1). There were no obvious differences among the PLE spectra detected at different wavelengths, and the PL emission profiles were almost identical regardless of the excitation wavelengths, suggesting that hetrostructured QDs formed upon the ZnS shell growth in the presence of Mn dopant ions maintained the emission characteristics of the CdTe core, rather than the formation of any significant fraction of separate Mn-doped ZnS nanoparticles occurring.<sup>60</sup>

Representative TEM and HRTEM images of CdTe core QDs, CdTe/ZnS QDs and Mn-doped (4.7% Mn) CdTe/ZnS QDs are shown in Figure 2. Average diameters of  $3.7 \pm 0.5$  nm,  $4.3 \pm 0.6$  nm and  $4.3 \pm 0.6$  nm were estimated for the CdTe, CdTe/ZnS, and Mn-doped CdTe/ZnS QDs respectively, as illustrated by the corresponding size histograms (SI, Figure S2). Given the expected thickness of 0.312 nm for one monolayer of ZnS shell, the diameter of both the CdTe/ZnS and Mn-doped CdTe/ZnS QDs shown in Figure 2b,c increases by ~0.6 nm in comparison with that of the original CdTe core, which consequently corresponds to the formation of one monolayer of ZnS shell. Details of the calculation of the ZnS layer

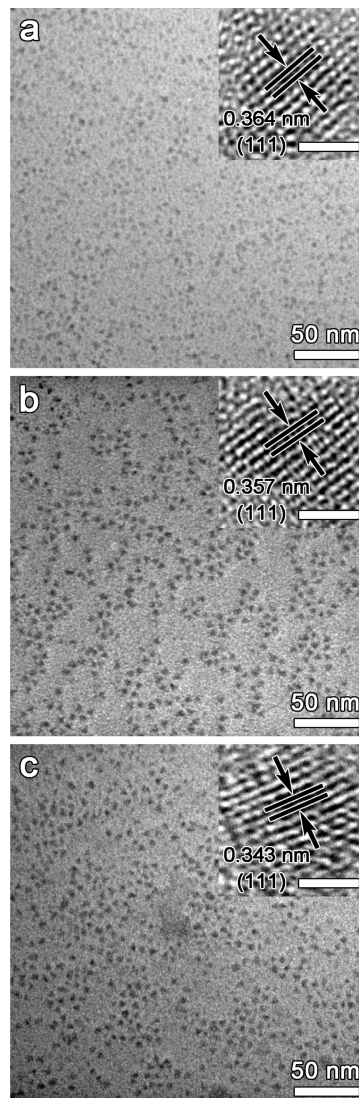


**Figure 2.** TEM and HRTEM (insets) images overlaid with identifications of crystalline planes showing the samples of (a) 3.7 nm CdTe QDs, (b) 4.3 nm CdTe/ZnS QDs, and (c) 4.3 nm Mn-doped (4.7%) CdTe/ZnS QDs. Scale bars in the insets correspond to 2 nm.

thicknesses for different samples based on the respective ICP-OES data are given in the SI (Table S1). The insets in Figure 2a–c show HRTEM images of representative single nanocrystals. For CdTe core QDs (inset in Figure 2a), an interplanar spacing of 0.364 nm was derived, in good agreement with the dominant (111) crystal lattice plane of bulk cubic zinc blende CdTe (0.370 nm). The interplanar spacing changed to 0.357 nm for CdTe/ZnS QDs (inset in Figure 2b) and to 0.343 nm for CdTe/ZnS QDs with manganese doping (inset in Figure 2c), which can be attributed to compression of the lattice planes in the CdTe core upon ZnS shell and the Mn-doped ZnS shell overgrowths,<sup>61</sup> in each case. Lattice planes in HRTEM images of CdTe/ZnS QDs and Mn-doped CdTe/ZnS QDs stretched across the entire nanocrystal with no evidence of discontinuity, which is consistent with epitaxial shell growth.<sup>62,63</sup>

The crystal structure of samples before and after ZnS shell growth was further analyzed by powder XRD (Figure 3). CdTe core QDs showed a diffraction pattern with peaks at  $2\theta$  of

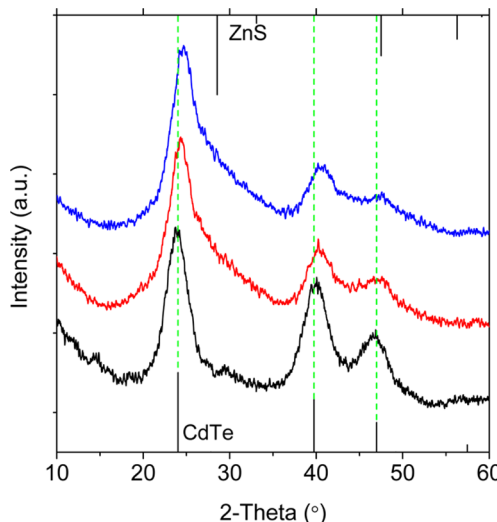


**Figure 3.** Powder X-ray diffraction patterns of CdTe QDs (black), CdTe/ZnS QDs (red), and Mn-doped (4.7%) CdTe/ZnS QDs (blue). Positions of XRD peaks for the zinc blende bulk CdTe (JCPDS No. 75-2086) and bulk ZnS (JCPDS No. 80-0020) are given by vertical solid lines shown below and above, respectively. Green lines are a guide for the eye.

23.9°, 40.1°, and 46.7°, corresponding closely to the (111), (220), and (311) reflections of cubic zinc blende bulk CdTe (shown as vertical lines). Upon shell formation, these peaks shifted to higher  $2\theta$  angles toward values corresponding to the ZnS phase, while maintaining the characteristic diffraction pattern of the zinc blende structure. Similar shifts in the diffraction patterns were observed during the growth of ZnS shells on CdSe cores by Dabbousi et al.<sup>63</sup>

**Optical Properties of Mn-Doped CdTe/ZnS QDs.** XRD data for Mn-doped QDs at different doping levels (SI, Figure S3) did not indicate any appreciable changes in the average sizes, approximated by the Scherrer equation. Thus, it is reasonable to discuss the optical properties of the Mn-doped QDs as a function of the Mn<sup>2+</sup> doping level at a nominal fixed QD size (4.3 nm). The manganese doping levels for the samples produced upon growth of a ZnS shell on CdTe cores in the presence of manganese ions were evaluated by ICP-OES and are summarized in Table 1. These results were obtained after thorough multistep purification of the QDs as outlined in the Experimental Section, in order to ensure that the determined amount of Mn<sup>2+</sup> ions did not include any remnants of those cations loosely bound to the surface of the QDs. The amount of Mn<sup>2+</sup> ions presumably incorporated into the ZnS

shell after 2 h of reflux consistently increased from 4.7% to 7.5% and further to 9.7% upon the increase of the initial feeding amounts of Mn<sup>2+</sup> precursor introduced into the reaction mixture. The average number of Mn<sup>2+</sup> dopant ions per single nanocrystal (Table 1) was estimated from the concentration of Cd<sup>2+</sup> and Mn<sup>2+</sup> from ICP-OES data (SI, Table S1) and the core size estimated from the absorbance spectra of the CdTe core,<sup>64</sup> and varies from 55 to 134 per QD. In order to determine the valence state of the Mn<sup>2+</sup> ions incorporated, XPS characterization was performed (SI, Figure S4), which showed that Mn 2p<sub>3/2</sub> signals for all three doping levels appeared at 641.6 ± 0.2 eV. This suggests that Mn<sup>2+</sup> ions were predominantly included in the Mn(II) state.<sup>65</sup>

The evolution of the optical parameters including PL QY, emission peak maximum ( $\lambda_{\text{max}}$ ), and full width at half-maximum (fwhm) of the emission peak, derived from the PL spectra of both undoped and Mn-doped CdTe/ZnS QDs with different initial feed amounts of Mn<sup>2+</sup> ions is presented in Figure 4. All samples were synthesized with the same initial concentration of Zn precursor ensuring the formation of an approximately one monolayer thin ZnS shell as discussed above but with varying amounts of Mn precursor. As shown in Figure 4a, the PL QY of CdTe/ZnS QDs with the lowest estimated amount of Mn dopant (4.7% after 2 h of reflux) first increased from 45% (for the core CdTe QDs) to 59% at the moment when the reaction system had just reached the reflux temperature of 100 °C (corresponding to time 0 min in Figure 4), then further increased to the maximum value of 62% after 10 min of reflux. This was then followed by a gradual decrease to 45% for longer reflux times. A similar trend was observed for CdTe/ZnS QDs, albeit with a stronger degree of PL QY decrease. For larger estimated amounts of dopant Mn<sup>2+</sup> ions (7.5% and 9.7% after 2 h of reflux), the PL QY showed a different trend, gradually decreasing with reflux time, when compared to the trend for the CdTe core (Figure 4a). This may be caused by the presence of some of the Mn<sup>2+</sup> ions at the CdTe/ZnS interface.<sup>3,66,67</sup>

As exemplified in Figure 4b,c, both the PL emission peak maximum ( $\lambda_{\text{max}}$ ) and the full width at half-maximum (fwhm) of the emission peaks of Mn-doped CdTe/ZnS QDs depended on the Mn<sup>2+</sup> concentration in the reaction mixture. However, the curves converged for prolonged reflux times which may indicate that Mn<sup>2+</sup> ions adsorbed on the CdTe surface in the initial reaction stages underwent a purification process during the ZnS shell growth, driven by the well-documented thermally activated diffusion of dopant ions into the shell under prolonged heating.<sup>3,4,67</sup> Furthermore, the observed narrowing of the PL fwhm (Figure 4c,d) for all samples during reflux suggests that simultaneous ZnS shell growth and inclusion of

**Table 1. Mn<sup>2+</sup> Doping Levels Determined from ICP-OES Analysis and the Corresponding Optical Properties of Mn-Doped CdTe/ZnS QDs**

initial Mn/Cd <sup>a</sup> (molar ratio)	Mn/Cd (molar ratio)	ICP-OES results		optical properties	
		Mn <sup>2+</sup> doping level <sup>b</sup> (mol %)	average Mn <sup>2+</sup> ions per QD	PL $\lambda_{\text{max}}$ (nm)	PL QY (%)
0 (CdTe)	N/A	N/A	N/A	610 ± 2	44.9 ± 2.2
0 (CdTe/ZnS)	N/A	N/A	N/A	652 ± 2	39.2 ± 2.0
0.108	0.060 ± 0.001	4.7 ± 0.1	55 ± 1	653 ± 2	45.4 ± 2.3
0.171	0.117 ± 0.002	7.5 ± 0.2	106 ± 2	653 ± 2	29.8 ± 1.5
0.297	0.148 ± 0.003	9.7 ± 0.2	134 ± 3	650 ± 2	9.7 ± 0.5

<sup>a</sup>Initial molar ratios of Mn/Cd are defined as the molar ratios of initial Mn<sup>2+</sup> precursor to [Cd]<sub>CdTe</sub> of CdTe QDs determined by ICP-OES. <sup>b</sup>Mn<sup>2+</sup> doping levels calculated from the molar ratio of [Mn]/([Mn] + [Cd]<sub>CdTe</sub> + [Zn]) measured by ICP-OES. The “average Mn<sup>2+</sup> ions doped per QD” values are calculated using the size of the CdTe core and the ratio of [Mn]/[Cd]<sub>CdTe</sub> from the ICP-OES data.

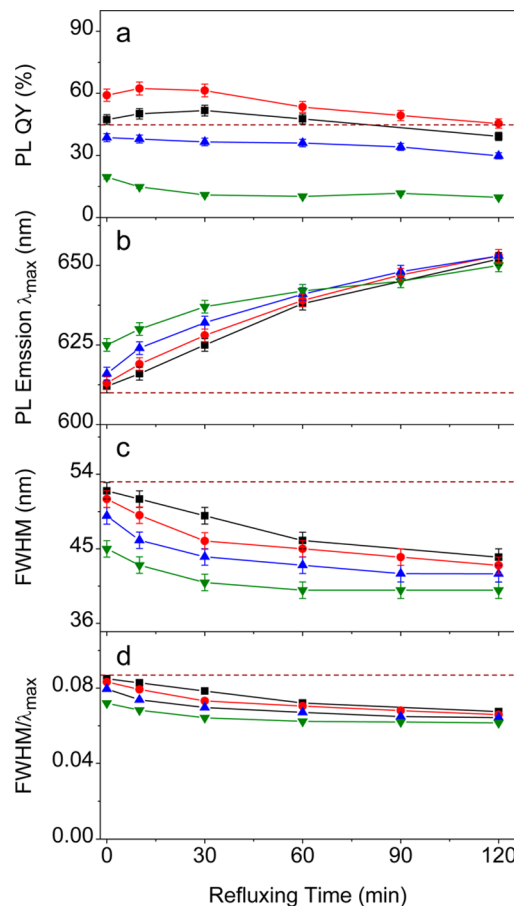


**Figure 4.** Temporal evolution (during reflux) of (a) PL QY, (b) PL peak maximum  $\lambda_{\text{max}}$ , (c) full width at half-maximum (fwhm) of PL peaks, and (d) the value of  $\text{fwhm}/\lambda_{\text{max}}$  of undoped CdTe/ZnS QDs (■), as well as Mn-doped CdTe/ZnS QDs with varying initial feed molar ratios of Mn<sup>2+</sup>-to-Cd<sup>2+</sup>: 0.108 (red circle), 0.171 (blue triangle), and 0.297 (green triangle). For reference, the corresponding values for CdTe QDs as starting core materials are shown as horizontal dashed lines in all panels. Reflux times do not include the time to reach the boiling point.

Mn<sup>2+</sup> ion dopants did not give rise to either size or composition distribution broadening for the particles in the ensemble.

For the majority of Mn<sup>2+</sup> doped Zn(S,Se) and CdS QDs, Mn<sup>2+</sup> states residing within the bandgap of the host QDs give rise to the orange Mn<sup>2+</sup> dopant emission centered around 585 nm, determined by the radiative transition from the first excited state  ${}^4\text{T}_1$  to the ground state  ${}^6\text{A}_1$ .<sup>19,27,68–71</sup> The intensity of this transition relies on efficient energy transfer from the excited excitonic states in the host QD material to the Mn dopant ions.<sup>72,73</sup> In the CdTe-based QDs studied here, the characteristic Mn<sup>2+</sup> dopant orange emission was not observed. This could be due to the absence of the above-mentioned energy transfer process,<sup>74,75</sup> as the emission maximum of the host CdTe nanocrystals was centered at 650 nm (Figure 1 and Table 1). This is lower in energy than the  ${}^6\text{A}_1 \rightarrow {}^4\text{T}_1$  absorption transition. In addition it may also be possible that the weaker emission of the Mn<sup>2+</sup> ions, even if present (at around 585 nm) overlapped with the stronger band-edge emission from the CdTe core and was masked by the latter. We note that for Mn-doped ZnS QDs (wide bandgap material) grown under similar conditions to the CdTe-based core/shell QDs, the weak orange

emission originating from the  ${}^4\text{T}_1 \rightarrow {}^6\text{A}_1$  transition of Mn<sup>2+</sup> ions was detected (SI, Figure S5).

Time-resolved PL measurements were further performed to reveal the nature and influence of various surface states involved in the emission processes. Figure 5a shows the PL

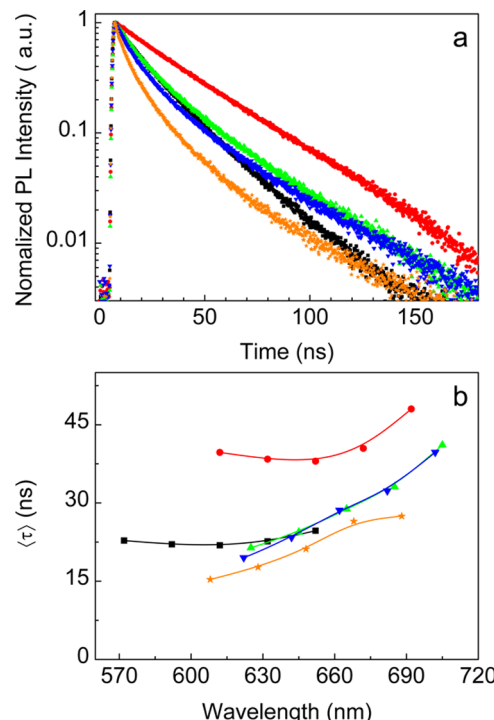


**Figure 5.** (a) Normalized time-resolved PL decay curves and (b) wavelength-dependent time-resolved PL average lifetimes for CdTe QDs (■), undoped CdTe/ZnS QDs (red circles), and Mn-doped CdTe/ZnS QDs with Mn<sup>2+</sup> doping levels of 4.7% Mn (green triangles), 7.5% Mn (blue triangles), and 9.7% Mn (orange stars). Systematic error is approximately  $\pm 0.5$  ns for all lifetime values.

decay curves measured at the PL emission peak ( $\lambda_{\text{max}}$ ) of undoped and Mn-doped CdTe/ZnS QDs. Since the decays of aqueous CdTe QDs are multiexponential,<sup>76</sup> the average lifetime (see the SI for definition) of the entire fluorescence decay process for CdTe and CdTe/ZnS QDs was determined from a two-exponential decay fit, while the best fits for the Mn-doped CdTe/ZnS QDs with varying doping levels were obtained from a three-exponential fit (all decay fitting data are summarized in Table S2 in the SI). In the case of the ZnS shell without Mn<sup>2+</sup> ions present, the average lifetime of 21.9 ns for CdTe QDs increased to 38.0 ns, indicating a reduction of the nonradiative decay rate. For the Mn-doped QDs, the average lifetimes were strongly dependent on the composition, decreasing to 28.8, 28.6, and 21.2 ns for CdTe/ZnS QDs with Mn<sup>2+</sup> doping levels of 4.7%, 7.5%, and 9.7%, respectively, compared to 38.0 ns for the undoped CdTe/ZnS QDs. As shown in Figure 5a, increasing the Mn<sup>2+</sup> doping level gave rise to an additional fast component with a decay time below 10 ns, implying an increased nonradiative decay rate, which may be associated with recombination through newly generated defect states from interfacial Mn<sup>2+</sup> dopant ions within the ZnS shell. In addition to PL decay lifetimes at the emission maximum peak wavelengths shown in Figure 5a, the spectrally resolved PL lifetimes for each sample detected over a broader range of wavelengths on the both sides of the peak's maximum are shown in Figure 5b. For

the CdTe QDs, the lifetimes exhibited far less wavelength-dependent behavior, compared with both undoped CdTe/ZnS QDs and Mn-doped CdTe/ZnS QDs, remaining relatively constant within the 21.9 to 24.7 ns time range. In contrast, the undoped CdTe/ZnS QDs already had a longer lifetime of 39.7 ns than the CdTe core QDs at the shortest detection wavelength, and showed a slight dip to 38.0 ns at the peak position, followed by an increase to 48.0 ns at the longest detection wavelength. The average lifetimes from the three-exponential analysis of the CdTe/ZnS:Mn QDs with doping levels of 4.7%, 7.5%, and 9.7% increased significantly with increasing detection wavelength, ranging from 21.4 to 41.1 ns, from 19.5 to 39.3 ns, and from 15.3 to 27.5 ns, respectively. These observations suggest that the fast decay channels involved in the emission processes of Mn-doped CdTe/ZnS QDs have a strong influence on the overall emission rate, in comparison with both CdTe QDs and undoped CdTe/ZnS QDs.

#### Magnetic Properties of Mn-Doped CdTe/ZnS QDs.

EPR measurements were carried out on Mn-doped CdTe/ZnS QDs to further determine the characteristics of the dopant's local environment. All the samples for EPR measurements were extensively purified as outlined in the Experimental Section and measured as concentrated dispersions in water. The EPR spectra of three samples with increasing Mn<sup>2+</sup> doping levels (4.7%, 7.5%, and 9.7%) are shown in Figure 6, along with the

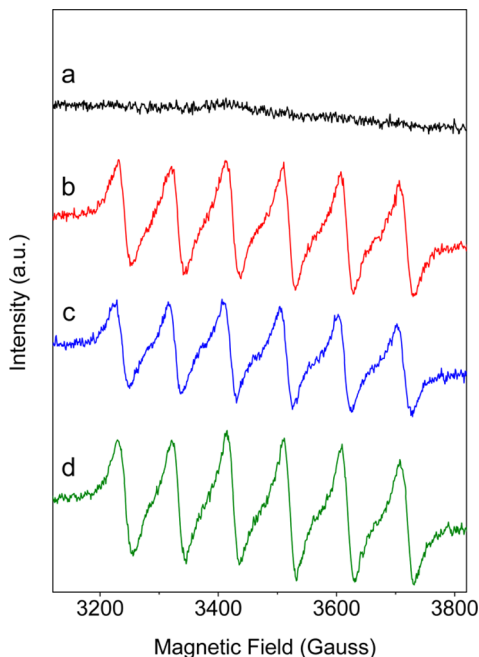


**Figure 6.** EPR spectra of (a) undoped CdTe/ZnS QDs and (b–d) Mn-doped CdTe/ZnS QDs with varying Mn<sup>2+</sup> doping levels of (b) 4.7%, (c) 7.5%, and (d) 9.7%, respectively.

reference EPR spectrum of undoped CdTe/ZnS QDs. The EPR spectra of all doped samples, regardless of the Mn doping level, are characterized by a six-line spectrum with a hyperfine splitting centered at  $H = 3.48$  kG ( $g \approx 2.005$ ), in contrast to undoped CdTe/ZnS QDs with only a flat background. The six line patterns are a signature of the electron–nuclear hyperfine coupling of Mn<sup>2+</sup> (nuclear spin  $I = 5/2$ ). Moreover, these sextet patterns indicate that Mn<sup>2+</sup> ions were spatially isolated, which excludes the formation of Mn<sup>2+</sup> ions clusters.<sup>77</sup> Furthermore,

the hyperfine splitting constant  $A$  values are close to  $90 \times 10^{-4}$  cm<sup>-1</sup>, which can be attributed to the fact that isolated Mn<sup>2+</sup> ions with different bonding environments are present near the surface region of QDs.<sup>19,37</sup> The nature of the hyperfine splitting reflects the covalency of the site occupied by the Mn<sup>2+</sup> ions and thus allows differentiation between Mn<sup>2+</sup> ions substituted within the nanocrystal lattice from other Mn<sup>2+</sup> ion based coordination compounds.<sup>36</sup> Thus, it is reasonable to expect that Mn<sup>2+</sup> ions located in the surface ionic or distorted sites should exhibit a larger hyperfine splitting than that of internal Mn<sup>2+</sup> ions inside the core.<sup>36,37</sup> Smaller hyperfine splitting values for Mn<sup>2+</sup> ions substituted for Zn<sup>2+</sup> and Cd<sup>2+</sup> ions in a covalently bound tetrahedral site in the cubic lattice would typically exhibit an average  $A$  value of  $64 \times 10^{-4}$  cm<sup>-1</sup> in bulk ZnS,<sup>78</sup> and  $57 \times 10^{-4}$  cm<sup>-1</sup> in bulk CdTe,<sup>79</sup> respectively, whereas values of  $A$  for Mn<sup>2+</sup> ions in a predominantly octahedral environment around  $90 \times 10^{-4}$  cm<sup>-1</sup> (similar to those measured here) have been attributed to ionic Mn<sup>2+</sup> (surface lattice bound Mn) or to Mn<sup>2+</sup> located in an interstitial site.<sup>80</sup> Since the QDs for EPR studies were extensively purified, surface ligand-bound Mn<sup>2+</sup> ions are not expected to be present in any significant amounts. Furthermore, hyperfine splitting constants of  $83 \times 10^{-4}$  cm<sup>-1</sup>,  $82.5$ – $87.6 \times 10^{-4}$  cm<sup>-1</sup>, and 90 G have been reported for the Mn-doped CdSe QDs,<sup>34</sup> InP QDs,<sup>37</sup> and CdS QDs,<sup>19</sup> respectively, similar to that observed herein. It was previously demonstrated that the core/shell structure of colloidal QDs (e.g., Mn<sup>2+</sup> doped CdSe/ZnS and CdS/ZnS) can significantly affect hyperfine splitting constant values.<sup>15,34</sup> In addition, Mn<sup>2+</sup> ions have been reported to possess high binding energies with the (001) facets of zinc blende II–VI nanocrystals<sup>3</sup> and be more readily doped into the Zn-based lattice than the Cd-based one, due to the smaller mismatch in ionic radii between Zn<sup>2+</sup> (0.74 Å) and Mn<sup>2+</sup> (0.80 Å) than that between Cd<sup>2+</sup> (0.97 Å) and Mn<sup>2+</sup>.<sup>81</sup> From the EPR results discussed above, the splitting value for our Mn-doped CdTe/ZnS QDs is similar to the  $A$  values observed for Mn<sup>2+</sup> located close to the QD surface rather than that in a bulk crystal.<sup>19,34</sup> As the size increase of the Mn-doped samples determined by TEM corresponds to approximately one monolayer of ZnS shell (Figure 2), the distribution pattern of the Mn<sup>2+</sup> ions can best be attributed to their doping into the thin ZnS shell rather than simply physisorbing them at the QD surface.<sup>82</sup> It has been previously shown for Mn-doped CdSe/ZnS QDs that the splitting value depends on the thickness of the shell, and that the decreasing hyperfine splitting indicates that the thicker shell provides a more ordered matrix for Mn<sup>2+</sup>.<sup>15</sup> Our EPR results appear to be consistent with well isolated Mn<sup>2+</sup> ions homogeneously distributed within the thin ZnS shell, where they substitute for Zn<sup>2+</sup> ions.

In addition to EPR measurements, since doped Mn<sup>2+</sup> ions acting as paramagnetic centers are expected to significantly affect MR signals which are dependent on the nuclear longitudinal relaxation of water protons, MR relaxivity measurements were performed in order to investigate the dopant's local environments and thus the ability of the doped QDs to shorten the longitudinal relaxation time ( $T_1$ ) of water protons. The  $T_1$  values of the CdTe/ZnS QDs with different Mn<sup>2+</sup> doping levels were measured on a 3.0 T MRI instrument at room temperature, and concentration-independent molar relaxivity  $r_1$  values were extracted by linear regression fitting of experimentally determined longitudinal relaxation rates ( $1/T_1$ ) of water protons versus the molar concentrations of Mn<sup>2+</sup> ions (ionic relaxivity,  $r_{1,Mn}$  (mM<sup>-1</sup> s<sup>-1</sup>), together with the molar concentrations of doped QD nanoparticles (QD particle

relaxivity,  $r_{1,QD}$  ( $\text{mM}^{-1} \text{s}^{-1}$ ). The data are presented in Figure 7a,b. For Mn-doped CdTe/ZnS QDs with doping levels of

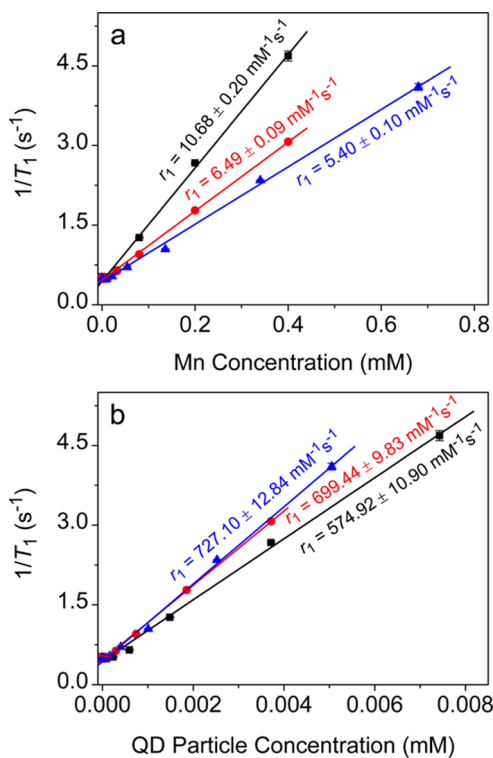


**Figure 7.** Experimentally determined data (solid symbols) and the corresponding linear fittings (solid lines) for  $T_1$  relaxation rates ( $1/T_1$ ) of water protons measured on a 3 T MRI clinical instrument, plotted against (a) the molar concentration of  $\text{Mn}^{2+}$  ions and (b) particle molar concentrations of Mn-doped CdTe/ZnS QDs with  $\text{Mn}^{2+}$  doping levels of 4.7% (■), 7.5% (red circle), and 9.7% (blue triangle), respectively.

4.7%, 7.5%, and 9.7%, ionic relaxivity  $r_{1,\text{Mn}}$  values were  $10.68 \pm 0.20$ ,  $6.49 \pm 0.09$ , and  $5.40 \pm 0.10 \text{ mM}^{-1} \text{s}^{-1}$ , respectively, while QD particle relaxivity  $r_{1,QD}$  values were  $574.92 \pm 10.90$ ,  $699.44 \pm 9.83$ , and  $727.10 \pm 12.84 \text{ mM}^{-1} \text{s}^{-1}$ , respectively. These values, measured at 3.0 T, were even larger than those obtained from manganese-based complexes in aqueous solution at low field strength (e.g., manganese dipyridoxal diphosphate,  $1.6 \text{ mM}^{-1} \text{s}^{-1}$  at 0.47 T),<sup>83–85</sup> which is interesting, considering the expectation that  $r_1$  values should increase with decreasing applied field strength.<sup>86</sup> In principle, paramagnetic centers shorten the longitudinal relaxation time of water protons nearby through the interactions between the electron spin of the paramagnetic center and water protons, giving rise to a faster recovery of the longitudinal magnetization of water protons.<sup>84</sup> Furthermore, according to the origin of paramagnetic relaxation enhancement of water protons, the exchangeable water surrounding the paramagnetic center can be typically divided into two separated regions: inner-sphere water and outer-sphere water.<sup>84,87</sup> The outer-sphere relaxation mainly refers to the relaxation enhancement of water molecules bonded to particles' surface ligands and their exchange with bulk water, while the inner-sphere proton relaxation mainly involves water molecules directly bonded to paramagnetic ions at the particle surface. In addition, the longitudinal relaxivity of water protons in the inner-sphere is strongly dependent on the tumbling time of the paramagnetic ions, and slowing the

tumbling of paramagnetic ions would favor higher  $r_1$  relaxivity.<sup>86–88</sup> In the current study, since all three samples have the same surface ligand, it is reasonable to expect that enhanced longitudinal relaxivities arise from inner-sphere relaxation. Thus, it can be further deduced that the high  $r_1$  values can be attributed to the slowed tumbling time of localized  $\text{Mn}^{2+}$  ions in the QDs, consequently giving rise to high relaxivity.<sup>15,83</sup> This is in line with the observations that the relaxivity of low molecular weight species such as manganese chelates can be increased by slowing their tumbling time, which is commonly achieved by the association of paramagnetic ions with large molecular weight species with strong binding interactions.<sup>83,88</sup> It is also worth noting that ionic relaxivity  $r_{1,\text{Mn}}$  values showed a monotonically decreasing dependence with increasing  $\text{Mn}^{2+}$  doping level, while QD particle relaxivity  $r_{1,QD}$  values increased with rising doping levels. Since the paramagnetic centers on the particle surface are major contributors to the relaxivity enhancement, increase of surface  $\text{Mn}^{2+}$  doping level will give rise to highly efficient interactions between the spins of water protons and  $\text{Mn}^{2+}$  ions, and consequently increased doping levels would lead to increased relaxivity. However, this effect could ultimately be partly counteracted at higher  $\text{Mn}^{2+}$  ion surface densities where Mn–Mn coupling would be enhanced.

The above observations suggest that the doping level-dependent behavior of the longitudinal relaxivities of water protons strongly depends on the paramagnetic  $\text{Mn}^{2+}$  ions doped on the QD surface, and provide strong indications that  $\text{Mn}^{2+}$  dopants were located within the thin single layer ZnS shell.<sup>15</sup>

## CONCLUSIONS

In summary, we have developed a synthetic strategy toward aqueous based core/shell colloidal QDs consisting of a CdTe core coated with a thin ZnS shell, which can be effectively doped by  $\text{Mn}^{2+}$  ions via their coprecipitation with  $\text{Zn}^{2+}$  ions using glutathione tripeptide as the sulfide ion source. Optical and magnetic studies provided strong indications that manganese dopant ions were homogeneously distributed within the thin monolayer-like ZnS shell. The shell not only improved the surface passivation of the CdTe QD cores leading to high (up to 45%) PL QYs of the resulting Mn-doped nanocrystals but also provided a suitable matrix for integration of varying amounts of  $\text{Mn}^{2+}$  ions with doping levels ranging from 4.7% to 9.7%, exhibiting high ionic relaxivity in the range of  $10.7\text{--}5.4 \text{ mM}^{-1} \text{s}^{-1}$  and rendering them promising dual fluorescent/paramagnetic probes. The current study on the rational design of core/(Mn-doped) shell QDs synthesized by the aqueous phase approach provides a simple and useful method toward Mn-doped fluorescent QDs to achieve high-quality dual-modality probes.

## ASSOCIATED CONTENT

### S Supporting Information

Size distribution histograms from TEM images in Figure 2; photoluminescence excitation spectra and PL emission spectra under varying excitation wavelengths for CdTe/ZnS QDs with  $\text{Mn}^{2+}$  doping level of 4.7%; XRD patterns of CdTe/ZnS QDs with varying  $\text{Mn}^{2+}$  doping levels; high resolution XPS spectra of Zn 2p and Mn 2p<sub>3/2</sub> of the CdTe/ZnS QDs with varying Mn doping levels; details of the calculation of the ZnS layer thickness; details of the calculation of average PL lifetimes and the decay fitting data for time-resolved photoluminescence

measurements. This material is available free of charge via the Internet at <http://pubs.acs.org>.

## AUTHOR INFORMATION

### Corresponding Author

\*E-mail: gaomy@iccas.ac.cn; andrey.rogach@cityu.edu.hk.

### Author Contributions

The manuscript was written through contributions of all authors. All authors have given approval to the final version of the manuscript.

### Notes

The authors declare no competing financial interest.

## ACKNOWLEDGMENTS

The authors thank the National Basic Research Program of China (2011CB935800), the National Nature Science Foundation of China (21203210, 81090271, and 21021003), and the Research Grant Council of Hong Kong S.A.R. (Project No. [T23-713/11]) for financial support.

## REFERENCES

- (1) Bussian, D. A.; Crooker, S. A.; Yin, M.; Brynda, M.; Efros, A. L.; Klimov, V. I. Tunable Magnetic Exchange Interactions in Manganese-Doped Inverted Core-Shell ZnSe-CdSe Nanocrystals. *Nat. Mater.* **2009**, *8*, 35–40.
- (2) Yu, J. H.; Liu, X. Y.; Kweon, K. E.; Joo, J.; Park, J.; Ko, K. T.; Lee, D.; Shen, S. P.; Tivakornsaithorn, K.; Son, J. S.; et al. Giant Zeeman Splitting in Nucleation-Controlled Doped CdSe:Mn<sup>2+</sup> Quantum Nanoribbons. *Nat. Mater.* **2010**, *9*, 47–53.
- (3) Erwin, S. C.; Zu, L. J.; Haftel, M. I.; Efros, A. L.; Kennedy, T. A.; Norris, D. J. Doping Semiconductor Nanocrystals. *Nature* **2005**, *436*, 91–94.
- (4) Norris, D. J.; Efros, A. L.; Erwin, S. C. Doped Nanocrystals. *Science* **2008**, *319*, 1776–1779.
- (5) Nag, A.; Sarma, D. D. White Light from Mn<sup>2+</sup>-Doped CdS Nanocrystals: A New Approach. *J. Phys. Chem. C* **2007**, *111*, 13641–13644.
- (6) Beaulac, R.; Schneider, L.; Archer, P. I.; Bacher, G.; Gamelin, D. R. Light-Induced Spontaneous Magnetization in Doped Colloidal Quantum Dots. *Science* **2009**, *325*, 973–976.
- (7) Alivisatos, A. P. Semiconductor Clusters, Nanocrystals, and Quantum Dots. *Science* **1996**, *271*, 933–937.
- (8) Resch-Genger, U.; Grabolle, M.; Cavaliere-Jaricot, S.; Nitschke, R.; Nann, T. Quantum Dots Versus Organic Dyes as Fluorescent Labels. *Nat. Methods* **2008**, *5*, 763–775.
- (9) Medintz, I. L.; Uyeda, H. T.; Goldman, E. R.; Mattoussi, H. Quantum Dot Bioconjugates for Imaging, Labelling and Sensing. *Nat. Mater.* **2005**, *4*, 435–446.
- (10) Gao, X. H.; Cui, Y. Y.; Levenson, R. M.; Chung, L. W. K.; Nie, S. M. In Vivo Cancer Targeting and Imaging with Semiconductor Quantum Dots. *Nat. Biotechnol.* **2004**, *22*, 969–976.
- (11) Murray, C. B.; Norris, D. J.; Bawendi, M. G. Synthesis and Characterization of Nearly Monodisperse CdE (E = Sulfur, Selenium, Tellurium) Semiconductor Nanocrystallites. *J. Am. Chem. Soc.* **1993**, *115*, 8706–8715.
- (12) Lee, J. A.; Mardanyi, S.; Hung, A.; Rhee, A.; Klostranec, J.; Mu, Y.; Li, D.; Chan, W. C. W. Toward the Accurate Read-out of Quantum Dot Barcodes: Design of Deconvolution Algorithms and Assessment of Fluorescence Signals in Buffer. *Adv. Mater.* **2007**, *19*, 3113–3118.
- (13) Chan, W. C. W.; Nie, S. M. Quantum Dot Bioconjugates for Ultrasensitive Nonisotopic Detection. *Science* **1998**, *281*, 2016–2018.
- (14) Santra, S.; Yang, H. S.; Holloway, P. H.; Stanley, J. T.; Mericle, R. A. Synthesis of Water-Dispersible Fluorescent, Radio-Opaque, and Paramagnetic CdS:Mn/ZnS Quantum Dots: A Multifunctional Probe for Bioimaging. *J. Am. Chem. Soc.* **2005**, *127*, 1656–1657.
- (15) Wang, S.; Jarrett, B. R.; Kauzlarich, S. M.; Louie, A. Y. Core/Shell Quantum Dots with High Relaxivity and Photoluminescence for Multimodality Imaging. *J. Am. Chem. Soc.* **2007**, *129*, 3848–3856.
- (16) Louie, A. Y. Multimodality Imaging Probes: Design and Challenges. *Chem. Rev.* **2010**, *110*, 3146–3195.
- (17) Koole, R.; Mulder, W. J. M.; Van Schooneveld, M. M.; Strijkers, G. J.; Meijerink, A.; Nicolay, K. Magnetic Quantum Dots for Multimodal Imaging. *Wiley Interdiscip. Rev.: Nanomed. Nanobiotechnol.* **2009**, *1*, 475–491.
- (18) Yang, Y. A.; Chen, O.; Angerhofer, A.; Cao, Y. C. Radial-Position-Controlled Doping in CdS/ZnS Core/Shell Nanocrystals. *J. Am. Chem. Soc.* **2006**, *128*, 12428–12429.
- (19) Nag, A.; Sapra, S.; Nagamani, C.; Sharma, A.; Pradhan, N.; Bhat, S. V.; Sarma, D. D. A Study of Mn<sup>2+</sup> Doping in CdS Nanocrystals. *Chem. Mater.* **2007**, *19*, 3252–3259.
- (20) Pradhan, N.; Peng, X. G. Efficient and Color-Tunable Mn-Doped ZnSe Nanocrystal Emitters: Control of Optical Performance Via Greener Synthetic Chemistry. *J. Am. Chem. Soc.* **2007**, *129*, 3339–3347.
- (21) Nag, A.; Chakraborty, S.; Sarma, D. D. To Dope Mn<sup>2+</sup> in a Semiconducting Nanocrystal. *J. Am. Chem. Soc.* **2008**, *130*, 10605–10611.
- (22) Zheng, J. J.; Yuan, X.; Ikezawa, M.; Jing, P. T.; Liu, X. Y.; Zheng, Z. H.; Kong, X. G.; Zhao, J. L.; Masumoto, Y. Efficient Photoluminescence of Mn<sup>2+</sup> Ions in MnS/ZnS Core/Shell Quantum Dots. *J. Phys. Chem. C* **2009**, *113*, 16969–16974.
- (23) Zeng, R. S.; Zhang, T. T.; Dai, G. Z.; Zou, B. S. Highly Emissive, Color-Tunable, Phosphine-free Mn:ZnSe/ZnS Core/Shell and Mn:ZnSeS Shell-Alloyed Doped Nanocrystals. *J. Phys. Chem. C* **2011**, *115*, 3005–3010.
- (24) Bol, A. A.; Meijerink, A. Luminescence Quantum Efficiency of Nanocrystalline ZnS: Mn<sup>2+</sup>. 2. Enhancement by UV Irradiation. *J. Phys. Chem. B* **2001**, *105*, 10203–10209.
- (25) Murase, N.; Jagannathan, R.; Kanematsu, Y.; Watanabe, M.; Kurita, A.; Hirata, K.; Yazawa, T.; Kushida, T. Fluorescence and EPR Characteristics of Mn<sup>2+</sup>-Doped ZnS Nanocrystals Prepared by Aqueous Colloidal Method. *J. Phys. Chem. B* **1999**, *103*, 754–760.
- (26) Ladizhansky, V.; Hodes, G.; Vega, S. Surface Properties of Precipitated CdS Nanoparticles Studied by NMR. *J. Phys. Chem. B* **1998**, *102*, 8505–8509.
- (27) Norris, D. J.; Yao, N.; Charnock, F. T.; Kennedy, T. A. High-Quality Manganese-Doped ZnSe Nanocrystals. *Nano Lett.* **2001**, *1*, 3–7.
- (28) Hanif, K. M.; Meulenberg, R. W.; Strouse, G. F. Magnetic Ordering in Doped Cd<sub>1-x</sub>Co<sub>x</sub>Se Diluted Magnetic Quantum Dots. *J. Am. Chem. Soc.* **2002**, *124*, 11495–11502.
- (29) Archer, P. I.; Santangelo, S. A.; Gamelin, D. R. Direct Observation of SP-D Exchange Interactions in Colloidal Mn<sup>2+</sup>- and Co<sup>2+</sup>-Doped CdSe Quantum Dots. *Nano Lett.* **2007**, *7*, 1037–1043.
- (30) Bhargava, R. N.; Gallagher, D.; Hong, X.; Nurmiikko, A. Optical-Properties of Manganese-Doped Nanocrystals of ZnS. *Phys. Rev. Lett.* **1994**, *72*, 416–419.
- (31) Bol, A. A.; Meijerink, A. Luminescence Quantum Efficiency of Nanocrystalline ZnS: Mn<sup>2+</sup>. 1. Surface Passivation and Mn<sup>2+</sup> Concentration. *J. Phys. Chem. B* **2001**, *105*, 10197–10202.
- (32) Srivastava, B. B.; Jana, S.; Karan, N. S.; Paria, S.; Jana, N. R.; Sarma, D. D.; Pradhan, N. Highly Luminescent Mn-Doped ZnS Nanocrystals: Gram-Scale Synthesis. *J. Phys. Chem. Lett.* **2010**, *1*, 1454–1458.
- (33) Beaulac, R.; Archer, P. I.; Ochsenbein, S. T.; Gamelin, D. R. Mn<sup>2+</sup>-Doped CdSe Quantum Dots: New Inorganic Materials for Spin-Electronics and Spin-Photonics. *Adv. Funct. Mater.* **2008**, *18*, 3873–3891.
- (34) Mikulec, F. V.; Kuno, M.; Bennati, M.; Hall, D. A.; Griffin, R. G.; Bawendi, M. G. Organometallic Synthesis and Spectroscopic Characterization of Manganese-Doped CdSe Nanocrystals. *J. Am. Chem. Soc.* **2000**, *122*, 2532–2540.



- (75) Seufert, J.; Bacher, G.; Scheibner, M.; Forchel, A.; Lee, S.; Dobrowolska, M.; Furdyna, J. K. Dynamical Spin Response in Semimagnetic Quantum Dots. *Phys. Rev. Lett.* **2002**, *88*.
- (76) Kapitonov, A. M.; Stupak, A. P.; Gaponenko, S. V.; Petrov, E. P.; Rogach, A. L.; Eychmüller, A. Luminescence Properties of Thiol-stabilized CdTe Nanocrystals. *J. Phys. Chem. B* **1999**, *103*, 10109–10113.
- (77) Sapra, S.; Nanda, J.; Anand, A.; Bhat, S. V.; Sarma, D. D. Optical and Magnetic Properties of Manganese-Doped Zinc Sulfide Nano-clusters. *J. Nanosci. Nanotechnol.* **2003**, *3*, 392–400.
- (78) Walsh, W. M., Jr. Effects of Hydrostatic Pressure on the Paramagnetic Resonance Spectra of Several Iron Group Ions in Cubic Crystals. *Phys. Rev.* **1961**, *122*, 762–771.
- (79) Ludwig, G. W.; Woodbury, H. H. *Electron Spin Resonance in Semiconductors*. In *Solid State Physics*; Academic Press: New York, 1962; Vol. 13.
- (80) Vangisbergen, S. J. C. H. M.; Godlewski, M.; Gregorkiewicz, T.; Ammerlaan, C. A. J. Magnetic-Resonance Studies of Interstitial Mn in GaP and GaAs. *Phys. Rev. B* **1991**, *44*, 3012–3019.
- (81) Radovanovic, P. V.; Gamelin, D. R. Electronic Absorption Spectroscopy of Cobalt Ions in Diluted Magnetic Semiconductor Quantum Dots: Demonstration of an Isocrystalline Core/Shell Synthetic Method. *J. Am. Chem. Soc.* **2001**, *123*, 12207–12214.
- (82) Borse, P. H.; Srinivas, D.; Shinde, R. F.; Date, S. K.; Vogel, W.; Kulkarni, S. K. Effect of Mn<sup>2+</sup> Concentration in ZnS Nanoparticles on Photoluminescence and Electron-Spin-Resonance Spectra. *Phys. Rev. B* **1999**, *60*, 8659–8664.
- (83) Kueny-Stotz, M.; Garofalo, A.; Felder-Flesch, D. Manganese-Enhanced MRI Contrast Agents: From Small Chelates to Nanosized Hybrids. *Eur. J. Inorg. Chem.* **2012**, 1987–2005.
- (84) Lauffer, R. B. Paramagnetic Metal-Complexes as Water Proton Relaxation Agents for NMR Imaging - Theory and Design. *Chem. Rev.* **1987**, *87*, 901–927.
- (85) Nordhøy, W.; Anthonsen, H. W.; Bruvold, M.; Brurok, H.; Skarra, S.; Krane, J.; Jynge, P. Intracellular Manganese Ions Provide Strong T1 Relaxation in Rat Myocardium. *Magnet. Reson. Med.* **2004**, *52*, 506–514.
- (86) Caravan, P.; Farrar, C. T.; Frullano, L.; Uppal, R. Influence of Molecular Parameters and Increasing Magnetic Field Strength on Relaxivity of Gadolinium- and Manganese-based T(1) Contrast Agents. *Contrast Media Mol. Imaging* **2009**, *4*, 89–100.
- (87) Caravan, P. Protein-Targeted Gadolinium-based Magnetic Resonance Imaging (MRI) Contrast Agents: Design and Mechanism of Action. *Acc. Chem. Res.* **2009**, *42*, 851–862.
- (88) Caravan, P.; Ellison, J. J.; McMurry, T. J.; Lauffer, R. B. Gadolinium(III) Chelates as MRI Contrast Agents: Structure, Dynamics, and Applications. *Chem. Rev.* **1999**, *99*, 2293–2352.